

Infrared Spectra of Pyroxenes (Crystalline Chain Silicates) at Room Temperature

J. E. Bowey,^{1*} A. M. Hofmeister² & E. Keppel²

¹ School of Physics and Astronomy, Cardiff University, Queen's Buildings, The Parade, Cardiff, Wales, CF24 3AA

² Department of Earth and Planetary Sciences, Washington University, 1 Brookings Drive, St. Louis MO 63130, USA.

Accepted XXX. Received YYY; in original form ZZZ

ABSTRACT

Crystals of pyroxene are common in meteorites but few compositions have been recognized in astronomical environments due to the limited chemistries included in laboratory studies. We present quantitative room-temperature spectra of 17 Mg–Fe– and Ca–bearing ortho- and clinopyroxenes, and a Ca-pyroxenoid in order to discern trends indicative of crystal structure and a wide range of composition. Data are produced using a Diamond Anvil Cell: our band strengths are up to 6 times higher than those measured in KBr or polyethylene dispersions, which include variations in path length (from grain size) and surface reflections that are not addressed in data processing. Pyroxenes have varied spectra: only two bands, at 10.22 μm and 15.34 μm in enstatite (En₉₉), are common to all. Peak-wavelengths generally increase as Mg is replaced by Ca or Fe. However, two bands in MgFe-pyroxenes shift to shorter wavelengths as the Fe component increases from 0 to 60 per cent. A high-intensity band shifts from 11.6 μm to 11.2 μm and remains at 11.2 μm as Fe increases to 100 per cent; it resembles an astronomical feature normally identified with olivine or forsterite. The distinctive pyroxene bands between 13 and 16 μm show promise for their identification in *Mid-Infrared-Instrument (MIRI)* spectra obtained with the *James Webb Space Telescope (JWST)*. The many pyroxene bands between 40 and 80 μm could be diagnostic of silicate mineralogy if data were obtained with the proposed *Space Infrared Telescope for Cosmology and Astrophysics (SPICA)*. Our data indicate that comparison between room-temperature laboratory bands for enstatite and cold $\sim 10\text{--}K$ astronomical dust features at wavelengths $\geq 28\ \mu\text{m}$ can result in the identification of (Mg,Fe)-pyroxenes that contain 7–15 per cent less Fe– than their true values because some temperature shifts mimic some compositional shifts. Therefore some astronomical silicates may contain more Fe, and less Mg, than previously thought.

Key words: line: identification – techniques: spectroscopic – stars: circumstellar matter – dust, extinction – ISM: lines and bands – infrared: general

1 INTRODUCTION

Silicate dust is ubiquitous in galaxies; before the mid-1990s amorphous, or glassy, submicron-sized silicate grains were assigned as carriers of broad strong absorption and emission bands centred at 10 and 18 μm in dusty environments including the envelopes of evolved stars, the interstellar medium and comets. Later small fractions of crystalline silicates were tentatively identified in oxygen-rich circumstellar environments (Waters et al. 1996) and firmly identified in comets (Wooden et al. 1999) and young stellar objects (YSOs) (Malfait et al. 1998) in far-IR spectra obtained by ESA's *Infrared*

Space Observatory Satellite. More recently, *Spitzer Infrared Spectrograph (IRS)* spectra have revealed crystalline silicate absorption bands in ultra-luminous IR galaxies (Spoon et al. 2006) and OH-megamaser galaxies (Willett et al. 2011). A systematic search of 7.5–38 μm *Spitzer* spectra for crystalline silicates finds that 868 spectra of 790 sources including early-type stars, evolved stars and galaxies contain crystalline silicates (Chen et al. 2016); spectra show evidence of olivine (forsterite), pyroxene (enstatite) or other unidentified crystalline minerals. However, many of these identifications are tentative because relatively few minerals have been compared with astronomical spectra despite the wide variety of crystalline silicates found in meteorites and on Earth (see e.g. Bowey & Adamson 2002, for a fuller discussion).

* E-mail: boweyj@cardiff.ac.uk

Astronomical grains are mostly expected to be magnesium-rich; whilst this is likely, laboratory data for magnesium-poor chemical compositions are limited to one or two compositions (e.g. [Tamanai, Mutschke & Blum 2009](#)) and the spectra not readily available, so alternatives have not been much explored by astrophysicists. [Bowey & Adamson](#) took a different approach, and matched relatively smooth astronomical $10\mu\text{m}$ profiles with a mixture of crystalline silicates with a relatively small component of amorphous silicate. By this analysis, the enhanced breadth of the $10\text{-}\mu\text{m}$ features in the circumstellar discs surrounding young stars and in molecular clouds could be reproduced by a mixture of crystalline pyroxenes with varying stoichiometries (80 per cent by mass) and amorphous silicates (20 per cent) but the laboratory data and ground-based data were of insufficiently high quality to rigorously test this hypothesis. Recently, [Do-Duy et al. \(2020\)](#) have proposed that the enhanced breadth of the $10\text{ }\mu\text{m}$ feature in molecular clouds and young stellar objects is due the presence of a few per cent of crystalline silicate dust (forsterite). The potential of mixtures of other crystalline silicate groups contributing has not been considered recently, even though the meteoritic record indicates a wide variety of crystalline silicates are present in at least some of these environments. Pyroxenes are a likely candidate because they are amongst the most common silicates in the most primitive meteorites.

1.1 Laboratory studies

Transmission spectra of pyroxenes embedded in KBr or polyethylene pellets have been previously published by [Ferraro \(1982\)](#), [Jäger et al. \(1998\)](#) and [Chihara et al. \(2002\)](#) but laboratory studies in the astronomical literature contain a relatively limited range of compositions including magnesium and iron: 4 Mg-rich Mg–Fe-pyroxenes ([Jäger et al. 1998](#)), 7 Mg-rich and 1 Fe-pyroxene ([Chihara et al. 2002](#)). Micro-spectroscopic and chemical techniques have been used to obtain 8–17- μm spectra of individual meteoritic grains, covering the Mg-rich end of the series ([Bowey et al. 2007](#)). We present new spectra of 8 Mg- and Fe-bearing orthopyroxenes, 9 Mg-, Ca- and Fe-bearing clinopyroxenes, and one Ca-bearing pyroxenoid obtained at room temperature over the wavelength range of the fundamental infrared bands for the range of chemistries extant in these solid-solution series.

Data were collected from powdered samples compressed in a diamond anvil cell (DAC) in order to form thin films of uniform thickness with minimal spaces between the grains (no embedding medium is used). Compressing the powder reduces the effect of scattering because the reflection at grain boundaries is minimized. Grain-sizes are deduced experimentally, to give the sharpest and most repeatable infrared bands ([Hofmeister, Keppel & Speck 2003](#)). Excess pressure is released prior to measuring the spectra so that the cell acts only as a sample-holder (see [Hofmeister, Keppel & Speck](#) and references therein for the detailed methodology). The method produces nearly perfect absorption spectra similar to those derived from the reflectivity of single crystals, with only slight rounding of the strongest peaks.

Our wavelength-absorption coefficients can be used as an optical depth profile and directly compared with astronomical observations of optically-thin emission, and foreground absorption in the infrared in order to derive the

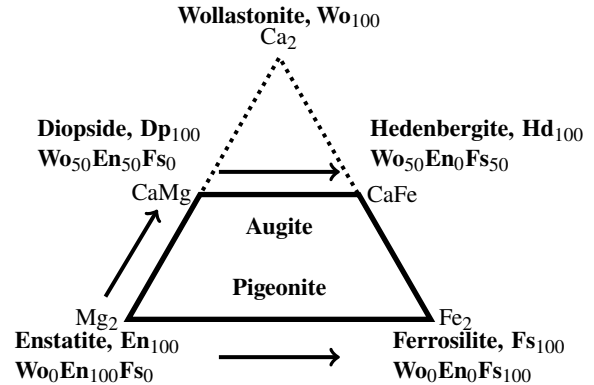


Figure 1. Nomenclature and metal components of pyroxenes, chain silicates of formula $[\text{Metal}]_2\text{-Si}_2\text{O}_6$: solid-solution series studied in this paper are Enstatite–Ferrosilite (En–Fs orthopyroxenes), and monoclinic pyroxenes in the Enstatite–Diopside (En–Dp) and Diopside–Hedenbergite (Dp–Hd) series; pigeonite and augite have intermediate Mg/Fe ratios with increasing Ca content. Wollastonite is a pyroxenoid.

chemical and temperature properties of the dust¹; once these factors are better constrained reflectivity studies of a narrower range of species can be used to deduce grain sizes and shapes from weak spectral peaks. Room-temperature DAC spectra are available for olivines ([Pitman et al. 2010](#)), hydrosilicates ([Hofmeister & Bowey 2006](#)), silicate overtones ([Bowey & Hofmeister 2005](#)) and glasses ([Speck, Wittington & Hofmeister 2011](#)).

To encourage consistent nomenclature between the disciplines of mineralogy, astrophysics and chemistry, we describe the mineralogical nomenclature of pyroxenes in Section 2; the samples, experimental and data processing details are in Section 3 where we also discuss the Diamond Anvil Cell (DAC) technique and present a method for estimating absorption coefficients from thin films of compressed powder. The complete spectra are presented in frequency units in Section 4, and detailed compositional-wavelength shifts are discussed and quantified in Section 5. The new data are compared with published room-temperature and low-temperature particulate spectra in Section 7. The data and initial astronomical implications are summarised in Section 8.

2 PYROXENES

Pyroxenes are chain silicates, characterized by chains of SiO_4 tetrahedra which are linked along the crystallographic c-

¹ An alternative method is to use absorption coefficients from indices of refraction, however, infrared spectra of strong spectral features calculated from refractive indices are often wavelength-shifted in relation to those of the laboratory spectra of particulates (e.g. [Jäger et al. 1998](#); [Bohren & Huffman 1983](#); [Sogawa et al. 2006](#)). Problems with particulate data have been resolved, or shown to be due to misunderstandings of mineralogy and problems with the laboratory technique ([Speck, Hofmeister & Barlow 1999](#); [Hofmeister, Keppel & Speck 2003](#); [Imai, et al. 2009](#); [Bowey, Adamson & Speck 2000](#)).

Table 1. Sample descriptions of the 18 minerals studied. For the natural samples, the chemical formulae are computed from electron microprobe analyses obtained from similar samples at the same locality, the formulation of the synthetics is described in the references. Mass density, ρ , is required for the derivation of mass extinction coefficients (see Section 3.3, equation 2) from the measured natural log absorption coefficients described in Section 3.2, equation 3.

Sample	Chemical Formula	Ref.	Locality	(Source ^a)	ρ gcm ⁻³
Enstatite–Ferrosilite Series (Orthopyroxenes): Fe²⁺ substitution for Mg²⁺					
En99	(Mg _{1.98} Ca _{0.02} Fe _{0.01})Si ₂ O ₆	<i>bc</i>	Norton Co. Aubrite meteorite	(SM)	3.21
En92	(Mg _{1.84} Fe _{0.11} Cr _{0.01} Ni _{0.01} Al _{0.01} Ca _{0.01})(Al _{0.03} Si _{1.97})O ₆	<i>b d</i>	Webster, Jackson, NC	(WU)	3.26
En90	(Mg _{1.80} Fe _{0.15} Ca _{0.02} Al _{0.02})(Al _{0.01} Si _{1.99})O ₆	<i>b</i>	Mogok, Burma	(Gemwow)	3.28
En85	(Mg _{1.70} Fe _{0.28} Ca _{0.01})Si ₂ O ₆	<i>eb</i>	Bamble ^f , Norway	(Wards)	3.32
En55	(Mg _{1.10} Fe _{0.79} Ca _{0.07} Mn _{0.02} Al _{0.01} Ti _{0.01})Si _{2.0} O ₆	<i>e</i>	Summit Rock, OR	(Wards)	3.56
En40	(Mg _{0.80} Fe _{1.09} Mn _{0.1} Ca _{0.03})Si ₂ O ₆	<i>g</i>	Wilagedera, Ceylon	(SG)	3.68
En12	(Mg _{0.24} Fe _{1.7} Ca _{0.04} Al _{0.02})(Al _{0.02} Si _{1.98})O ₆	<i>e</i>	Greenland	(GRR)	3.90
En1	(Mg _{0.02} Fe _{1.79} Mn _{0.13} Ca _{0.03} Na _{0.01})Si ₂ O ₆	<i>h</i>	Lofoten, Norway	(GRR)	3.99
Enstatite–Diopside–Wollastonite Series (Clinopyroxenes): Ca²⁺ substitution for Mg²⁺					
Wo ₂₁ En ₇₉	Dp ₄₂ En ₅₈	<i>i</i>	Synthetic	(NJ)	3.3 ^d
Wo ₃₀ En ₇₀	Dp ₅₉ En ₄₁	<i>i</i>	Synthetic	(NJ)	3.3
Wo ₄₀ En ₆₀	Dp ₈₁ En ₁₉	<i>i</i>	Synthetic	(NJ)	3.3
Wo ₅₀ En ₅₀	Dp ₁₀₀	<i>i</i>	Synthetic	(NJ)	3.3
Wo ₉₉ En ₁	Ca _{1.98} (Mg _{0.02} Fe _{0.01} ³⁺)(Si _{1.99} Al _{0.01})O ₆	<i>d</i>	Crestmore, CA	(WU)	2.92
Diopside–Hedenbergite Series (Clinopyroxenes): Fe²⁺ substitution for Mg²⁺ with 50 per cent Ca²⁺					
Wo ₅₀ En ₄₇	(Ca _{0.99} Na _{0.03})(Mg _{0.94} Fe _{0.03} Al _{0.01})Si ₂ O ₆	<i>j</i>	DeKalb, NY	(NM)	3.3 ^d
Wo ₄₉ En ₃₆	(Ca _{0.99} Na _{0.01})(Mg _{0.73} Mn _{0.02} Fe _{0.25} Ti _{0.01} Al _{0.01})(Si _{1.95} Al _{0.05})O ₆	<i>g</i>	Calumet, CO	(WU)	3.4
Wo ₄₇ En ₆	Ca _{0.93} (Mg _{0.12} Mn _{0.04} Fe _{0.80} ²⁺ Fe _{0.06} ³⁺ Al _{0.02})(Si _{1.99} Al _{0.01})O ₆	<i>g</i>	Iona Is., Rockland, NY	(ExM)	3.5
Pigeonite					
Wo ₁₀ En ₆₂	Ca _{0.20} (Mg _{1.25} Fe _{0.54} Al _{0.02})(Si _{1.98} Al _{0.02})O ₆	<i>k</i>	Synthetic	(AT)	3.3
Wo ₃₆ En ₃₇	(Ca _{0.72} Na _{0.02})(Mg _{0.75} Mn _{0.01} Fe _{0.48} Ti _{0.03} Al _{0.01})(Si _{1.93} Al _{0.07})O ₆	<i>g</i>	Belmont Quarry, Loudon, VA	(ExM)	3.4 ^d

^a NJ = N. Johnson; NM = National Museum of Natural History sample #R18682; ExM = Excalibur Mineral Co.; AT = Alan Turnock; WU = Washington University; SM = Schooler’s Minerals; RFD = R. F. Dymek sample #72816; SG = S. Guggenheim; GRR = G. R. Rossman

^b See Hofmeister (2012) for microprobe analyses: The aubrite contains 5% microscopic diopside inclusions (blebs) of composition Mg_{1.10}Ca_{0.85}Na_{0.02}Al_{0.02}Si₂O₆ ≡ Wo₄₃En₅₅. The Mogok sample is a large, gem-quality single-crystal. Near-IR spectra of the O-H stretching bands and visible to ultraviolet spectra of the electronic transitions (e.g. Fe²⁺) are also provided of these materials.

^c Okada et al. (1988)

^d Deer, Howie & Zussman (1978); clinopyroxene and pigeonite mass densities, ρ are from tabulated values and are quoted to 3 significant figures if they are from the same locality, or to two significant figures if they are estimates based on a similar composition.

^e Goldman & Rossman (1979)

^f This is the sample incorrectly called ‘Bramble’ Enstatite in Bowey et al. (2001).

^g Microprobe analysis performed at Washington University; analysis in Table A2.

^h Sample #433 (Ormaasen 1977)

ⁱ Dp₅₉En₄₁ by decomposition of natural tremolite (Johnson & Fegley 2003), others with similar methodology but different starting compositions (Johnson 2002) and personal communication.

^j Hemingway et. al. (1998), Hofmeister & Pertermann (2008)

^k A. Turnock, personal communication; Huebner & Turnock (1980)

axis by shared oxygen atoms. The generic formula is (M2, M1)T₂O₆ where M2 refers to cations in a distorted octahedral coordination, M1 to cations in a regular octahedral coordination and T to tetrahedrally coordinated cations (usually Si⁴⁺) (Morimoto et al. 1988). The triangle in Figure 1 illustrates the nomenclature of chain silicates in the pyroxene and pyroxenoid groups, with the most common substitutions. Minerals in the quadrilateral at the bottom of the figure are denoted pyroxenes. In pyroxenes Mg²⁺, Fe²⁺ occupy M1 and M2 lattice sites whilst Ca²⁺ occupies only M2 sites. Pyroxenoids occur when Ca²⁺ occupies both M1 and M2 sites (i.e. Ca²⁺ occupancy of M1+M2 > 50 per cent), and the

chains are twisted with a repeat of 3 or more. Pyroxenoids are represented here by the Ca end-member, wollastonite (Ca₂Si₂O₆, Wo₁₀₀). Mineralogical formulae Wo_wEn_xFs_y are calculated from the atomic percent of each of Ca²⁺, En²⁺, and Fe²⁺, respectively; if no other elements were included $w + x + y \approx 100$.

We obtain spectra from samples listed in Table 1 representing three sides of the pyroxene quadrilateral because these minerals are abundant in terrestrial environments and in meteorites. Minerals are named according to the percentage of wollastonite and enstatite in the unit cell; the fer-

rosilite content can be deduced by subtraction or, more accurately, from the chemical formulae listed in the table.

(i) **The Enstatite ($\text{Mg}_2\text{Si}_2\text{O}_6$, En_{100}) – Ferrosilite ($\text{Fe}_2\text{Si}_2\text{O}_6$, Fs_{100}) Series** where Mg^{2+} is replaced by Fe^{2+} . In this orthopyroxene series the crystal axes are orthogonal to each other because Fe^{2+} and Mg^{2+} are of similar size. However, in circumstances of rapid crystallisation, one axis can be inclined giving rise to a clinoenstatite to clinofersilite series with similar compositions, but because these are rare in terrestrial samples they are beyond the scope of this paper. [Chihara et al.](#) found little difference between the infrared spectra of orthoenstatite and clinoenstatite at wavelengths shorter than 40 μm and significant differences at longer wavelengths (see Section 6.2).

(ii) **The Enstatite–Diopside–Wollastonite ($\text{Ca}_2\text{Si}_2\text{O}_6$; Wo_{100}) Clinopyroxene Series** where Mg^{2+} in the M2 site are replaced by larger Ca^{2+} cations. Pyroxenes comprise silicates with ≤ 50 per cent Ca^{2+} , thus diopside ($\text{CaMgSi}_2\text{O}_6$; $\text{Wo}_{50}\text{En}_{50}$, or Dp_{100}) is the end-member pyroxene; wollastonite, the end-member pyroxenoid is also included in this study because it appears in meteorites. The larger radius of Ca^{2+} changes the shape of the unit cell producing crystals with an inclined a -axis, giving rise to a monoclinic structure (clinopyroxenes).

(iii) **The Diopside – Hedenbergite ($\text{CaFeSi}_2\text{O}_6$; $\text{Wo}_{50}\text{En}_0$) Clinopyroxene Series** where Fe^{2+} replaces Mg^{2+} in the M1 site; these crystals are also monoclinic.

Two pigeonites, whose composition does not fall on the edges of the pyroxene quadrilateral, are also included to indicate some of the variety of terrestrial pyroxenes. Pigeonites are monoclinic pyroxenes with a relatively-low calcium content.

2.1 Effect of trace elements and impurities in natural samples

Natural samples tend to contain trace quantities of Cr, Ni, Mn, Ti and Na which replace $\lesssim 5$ per cent of the main constituents of the silicates. Although different cations theoretically affect the spectra, they do not normally do so at this level of substitution unless the impurity has a substantially different mass, charge or volume from the cation it replaces. By convention traces of Mn^{2+} and Ni^{2+} are summed with Fe^{2+} , because the cations are of similar size and are indistinguishable from Fe^{2+} in infrared spectra. Additional samples were measured that have chemical compositions only slightly different from those reported here, and their spectra were nearly identical.

Impurities appear as weak bands in regions that are transparent for the major composition. We found quartz impurities in our original En_1 and En_{12} spectra and subtracted them from our data (Appendix A1). Sample En_{99} is a good test case for less easily distinguishable impurities because the meteoritic sample is known to contain 5% of microscopic clinopyroxene inclusions (see Section 6.1), which is the canonical detectable limit. At higher $\gtrsim 10$ per cent concentrations impurities can also broaden bands and cause them to blend, the effect of substantial substitution of Al^{3+}

for Si^{4+} will be explored in a later paper. Here, we report data on samples with the smallest quantities of minor impurities to focus on effects of the major cation variations (Mg, Fe, and Ca) and we have found no evidence that impurities significantly affect the current data set.

3 EXPERIMENTAL METHODS

Samples are described in Table 1. The chemical formulae were computed from published chemical analysis of samples from the same locality, as cited, or from electron microprobe analysis performed at Washington University using a JEOL-733 equipped with Advance Microbeam automation. The accelerating voltage was 15 kV, beamcurrent was 30 nA, and beam diameter was 1 μm . X-ray matrix corrections were based on a modified [Armstrong \(1988\)](#) CITZAF routine. Silicates and oxides were used as primary standards.

IR absorption spectra were acquired using an evacuated Bomem DA 3.02 Fourier transform spectrometer with an accuracy of $\sim 0.01 \text{ cm}^{-1}$. An SiC source was used for the entire spectral range. The number of scans ranged from 500 to 2000. Far-IR spectra, from ~ 50 to 650 cm^{-1} (~ 200 – $15 \mu\text{m}$), were obtained at 1 – 2 cm^{-1} -resolution with an Si-bolometer and, in some cases a 12 μm coated mylar beamsplitter was used to provide higher throughput at the lowest frequencies. Mid-IR spectra from ~ 450 to 4000 cm^{-1} (~ 23 – $2.5 \mu\text{m}$) were obtained with a HgCdTe detector and a KBr beamsplitter and 1 – 2 cm^{-1} -resolution.

Samples were hand-ground for a maximum of 10 minutes in order to reduce the effects of crystal orientation without degrading the long-range crystal structure (see e.g. the study by [Imai, et al. 2009](#), for the spectroscopic effect of excessive mechanical grinding). However, pyroxenes tend to form elongated laths with the long axis parallel to their c -axes (the axes of the chains) and these tend to lie on their sides when compressed, the crystal orientation in the DAC will not be perfectly randomized. This effect will be offset slightly by the non-parallel condensing beam of the DAC, so that all the crystal axes are sampled.

Optically-thin, ~ 0.2 to $2 \mu\text{m}$ -thick, films were made by compressing powders in a diamond anvil cell (DAC) to form a uniform thickness by repeatedly applying ~ 10 kbar pressure for a few seconds. Excess pressure is released prior to measuring the spectra so that the cell acts as a sample-holder ([Hofmeister, Keppel & Speck](#), and references therein) and the crystals revert to their decompressed state by elastic decompression (see [Hofmeister et al. 1989](#), for decompression after applying hydrostatic pressures of up to $\lesssim 425$ kbar in olivine). Various powder thicknesses were used to confirm the existence of weak peaks, to ascertain that optically-thin conditions hold for the most intense peaks, and to minimize fringing in the transparent regions ([Hofmeister & Bowey 2006](#)).

Band strengths near 700 cm^{-1} were calibrated against a film whose thickness was determined by using a 1.93 μm -thick microphone foil as a spacer around an aperture containing a sample which had been finely ground under alcohol.

Aluminium microphone foils, nominally $2.5 \pm 0.5 \mu\text{m}$ - and $4 \mu\text{m}$ -thick, were purchased on ebay from Geisnote. Their thickness was checked by placing a strip of the thicker foil between two 25mm-diameter KBr discs. The absorp-

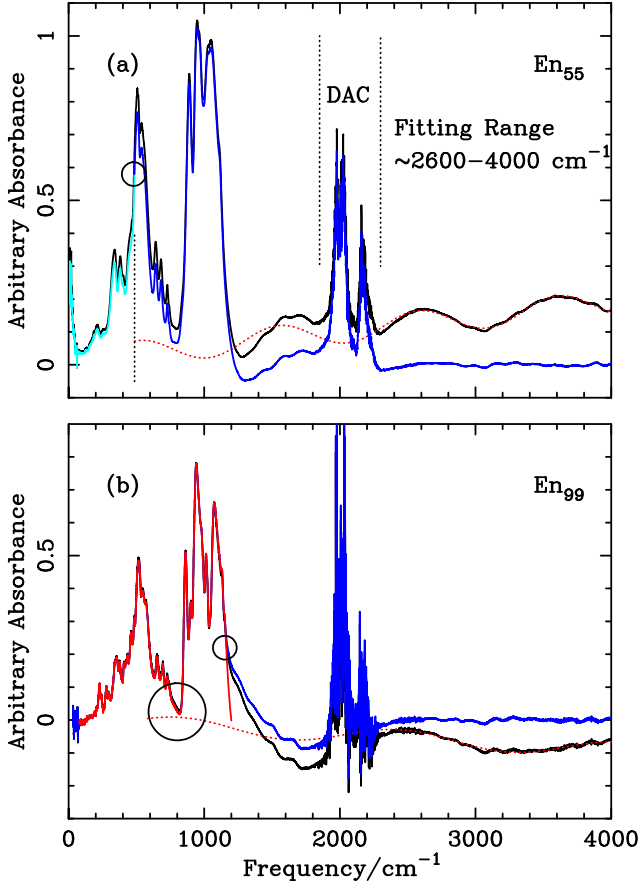


Figure 2. (a) The complete spectrum of En_{55} before defringing (black) with sinusoidal function fitted to 2600 to 4000 cm^{-1} -range (red-dotted). This was subtracted as far as the merging point near 580 cm^{-1} to produce the defringed spectrum. The low frequency region (cyan) was obtained by scaling a spectrum of another film to match the higher frequency spectrum. DAC denotes the region dominated by absorption within the diamond anvil cell. (b) Removing the wing near 1100 cm^{-1} : black - original spectrum, blue - after defringing, red after merging near 1100 cm^{-1} . Small circles indicate the merging points and the large circle highlights the transparent region whose level may be affected by unresolved weak peaks.

tion spectra showed fringes whose thickness is given by $B = 1/(2n\Delta\nu)$, where $\Delta\nu$ is the average spacing and n is the index of refraction $= 1$ for the air gap (Griffiths & deHaseth 1986). The nominally $4\text{-}\mu\text{m}$ foil, was found to be $5.3\text{ }\mu\text{m}$ thick. The thin single foil was below $2\text{ }\mu\text{m}$ thick because no fringes were seen. In order to move the interference into the measurable near-mid-infrared wavelength range, the thinner foil was doubled and the double-thickness measured to be $3.86\text{ }\mu\text{m}$ -thick.

3.1 Data processing

The $450\text{--}4000\text{-cm}^{-1}$ spectra contained underlying-fringes which were removed by fitting and subtracting a sloping sinusoidal function to the base line at frequencies higher than 2600 cm^{-1} (Figure 2(a)). Assuming that the absorbance is zero near zero frequency, the average level of the relatively

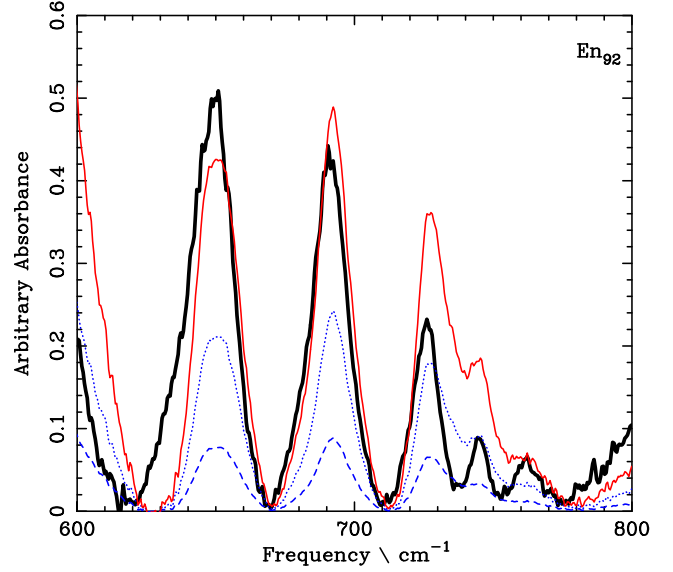


Figure 3. Calibrating the absorbance of En_{92} . Film of known thickness (thick black curve), uncalibrated En_{92} (blue dashed), En_{92} matched to $> 725\text{ cm}^{-1}$ bands (blue dotted), preferred match to $< 625\text{ cm}^{-1}$ peaks (solid red)

noisy $80\text{--}120\text{-cm}^{-1}$ -range was subtracted from the far-IR ($50\text{--}650\text{ cm}^{-1}$) spectra and then these were scaled to match the defringed mid-IR data.

The apparent broadening (or wing) of the $\geq 1100\text{-cm}^{-1}$ ($9.1\text{-}\mu\text{m}$)-region in some samples (Figure 2(b)) is not due to absorption. The wing is due to strong reflection at frequencies above the strongest Si-O stretching (LO) mode (see Wooten 1972), which reduces the measured transmission, while enhancing the perceived absorption. If the sample were negligibly thin, the wing would not exist. This effect is reduced in films in comparison with the spectra of dispersions, but is not completely absent because the films are slightly wedged. The wing was removed by scaling an exponential function modelled on the same, unaffected, region in En_{55} to the spectra affected and merging it with the good data at lower frequencies (Figure 2(b)). Spectra were subsequently trimmed to cover the region between 80 and 1200 cm^{-1} ($125\text{ }\mu\text{m}$ to $8.3\text{ }\mu\text{m}$) and normalised to the area under En_{55} between 80 and 1200 cm^{-1} since the area under the spectrum is proportional to the number of molecular-bonds responsible for the absorption features and that this should be the same for all the pyroxenes. These are the normalised laboratory absorbance spectra, (\bar{a} , calculated from a in Equation 1 below) used to determine the compositional dependence of the peak positions.

Uncertainties in the spectral shapes are more significant at the merging points near 500 cm^{-1} ($20\text{ }\mu\text{m}$), and there is remaining uncertainty in the intrinsic level of the baseline of the transparent regions near 80 cm^{-1} , $600\text{--}800\text{ cm}^{-1}$ and 1200 cm^{-1} . Additional measurements of the $600\text{--}800\text{-cm}^{-1}$ region of En_{92} for band strength calibration (Figure 3), indicate that there may be unresolved weak peaks near 800 cm^{-1} in some of the spectra which manifest as a change from a U-shape to a V-shape (e.g. in En_{99}

and En₉₂); they may also be due to the trace quantities of other cations listed in Table 1.

3.2 Band-strength calibration

Laboratory absorbance

$$a = -\log_{10} \frac{I_t}{I_*} = A \times d, \quad (1)$$

where I_t is the intensity of the beam transmitted through the DAC containing the sample and I_* is the intensity of the beam transmitted through the empty cell. a is equivalent to the absorption coefficient, A , times the film thickness d in the spectroscopic, chemical and mineralogical literature. However, astronomers use a natural log absorption coefficient (or optical depth, τ) units so our pyroxene data are presented as

$$\tau(\mu\text{m}^{-1}) = \frac{A}{d} \times 2.3026, \quad (2)$$

where the factor of 2.3026 is derived from the change of base formula.

Band strengths for the En–Fs series were estimated by subtracting a spline fit from the base of the weak peaks between 600–800 cm^{-1} region of En₉₂ and matching the areas of the two strongest peaks between 640 and 710 cm^{-1} to that of a film of known thickness (Figure 3).

The estimated thickness of the normalised En₉₂ spectrum was 0.35 μm and varying the frequency range of the area calculation indicated an uncertainty in d of about 0.02 μm or 6 per cent. Due to the prior normalisation to En₉₂, the actual thickness of the mid-infrared-film was $0.29 \pm 0.02 \mu\text{m}$. This procedure was then repeated for the Wo₅₀En₅₀ (Dp₁₀₀) sample and a film-thickness of 0.71 μm deduced. The natural log absorbance coefficients, τ , were obtained by scaling the normalised laboratory-absorbance spectra of the En–Fs orthopyroxenes to the En₉₂ thickness, and the En–Dp–Wo and Dp–Hd clinopyroxenes to the thickness of Dp₁₀₀.

Values of the calculated mid-infrared sample thicknesses are in Table A. Knowing the original thickness helps to gauge possible rounding of the peaks in overly thick films (e.g. Hofmeister, Keppel & Speck 2003). Each peak in a spectrum has an associated band strength and thus a range of sample thickness exists where the band is best observed.

3.3 Calculation of Mass Extinction Coefficients.

We present our data as natural log absorption coefficients because this represents attenuation and path length. Mass extinction coefficients, κ (cm^2g^{-1}), can be calculated using the relation

$$\kappa = 10^4 \tau / \rho \quad (3)$$

where ρ is the density of the mineral. Room-temperature orthopyroxene densities vary in a linear fashion with Mg:Fe ratio between 3.2 gcm^{-3} (En₁₀₀) and 4.00 gcm^{-3} (En₀) (Deer, Howie & Zussman 1978). Estimated densities for each of our samples are in Table 1.

4 OVERVIEW OF SPECTRA

The complete 80–1200 cm^{-1} spectra of the orthopyroxene, Enstatite–Ferrosilite series and the Enstatite–Diopside–Wollastonite and Diopside–Hedenbergite Series are displayed in Figure 4 along with two pigeonites and end-member wollastonite (dashed). In common with nearly all low-pressure silicates the spectra have strong Si–O stretching modes near 1000 cm^{-1} (10 μm) and O–Si–O-bending modes near 500 cm^{-1} due to their SiO₄ tetrahedra. Translations due to motions of the metal cations occur at frequencies below about 450 cm^{-1} . Chain silicates exhibit additional and distinctive weaker bands in the 600–800 cm^{-1} (16.5–12.5 μm) range due to Si–O–Si bending modes in the linked oxygen atoms of the chains of silicate tetrahedra.

As observed by others (e.g. Jäger et al. 1998; Chihara et al. 2002; Bowey et al. 2007), in the En–Fs series bands generally move to lower frequencies (longer wavelength, towards the red), as Mg is replaced with Fe, with larger frequency shifts occurring in the translational bands. In common with other solid-solution series, endmembers (En₉₉ and En₁) have more and sharper peaks than intermediate members. Several bands show dramatic changes when the Fe content exceeds ~ 50 per cent in behaviour analogous to that previously observed in the olivine series (Hofmeister & Pitman 2007); this effect will be discussed in Section 5. It is noteworthy that only two bands are observed to move to *higher* frequencies (to the blue) with an increase in Fe content, these shifts are small - frequencies shift between 862–893 cm^{-1} (11.6–11.2 μm) and 460–464 cm^{-1} (21.7–21.51 μm) and that both shifts occur only at the Mg-rich (~ En₁₀₀–En₄₀) end of the series. We generally identify similar bands and compositional trends to Chihara et al. (see Section 7).

As in the En–Fs series, bands in the Dp–Hd series shift to lower frequencies as Fe replaces Mg in the monoclinic Dp–Hd series; no bands shift to higher frequencies with an increase in Fe. Peaks in the En–Dp–Wo series shift to lower frequencies with replacement of Mg for Ca because the larger cation forces expansion of the lattice. The wollastonite spectrum resembles the En–Dp spectra above 400 cm^{-1} because these bands represent nearest-neighbour interactions. But, due to its different long-range order wollastonite, has a very different absorption profile in the 200–400- cm^{-1} region of the Translations. Spectra of the pigeonites are similar to pyroxenes on the nearest edges of the pyroxene-composition quadrilateral (Figure 1). For example, the effect of 10 per cent substitution of Ca for Mg in Wo₁₀En₆₂ reduces the number of narrow bands, but does not alter the spectrum much from the rest of the En–Fs series. In contrast, more substantial replacement of Mg and Fe by Ca in Wo₃₆En₃₇ noticeably reduces the height of the peak near 840 cm^{-1} , weakens the translations and adds an extra Si–O–Si band near 760 cm^{-1} in comparison to minerals in the Dp–Hd Series. Further discussion of pigeonites and wollastonite is beyond the scope of this paper.

5 COMPOSITION-DEPENDENT WAVELENGTH SHIFTS

In order to identify minerals in astronomical dust it is necessary to determine the degeneracy between wavelength-shifts

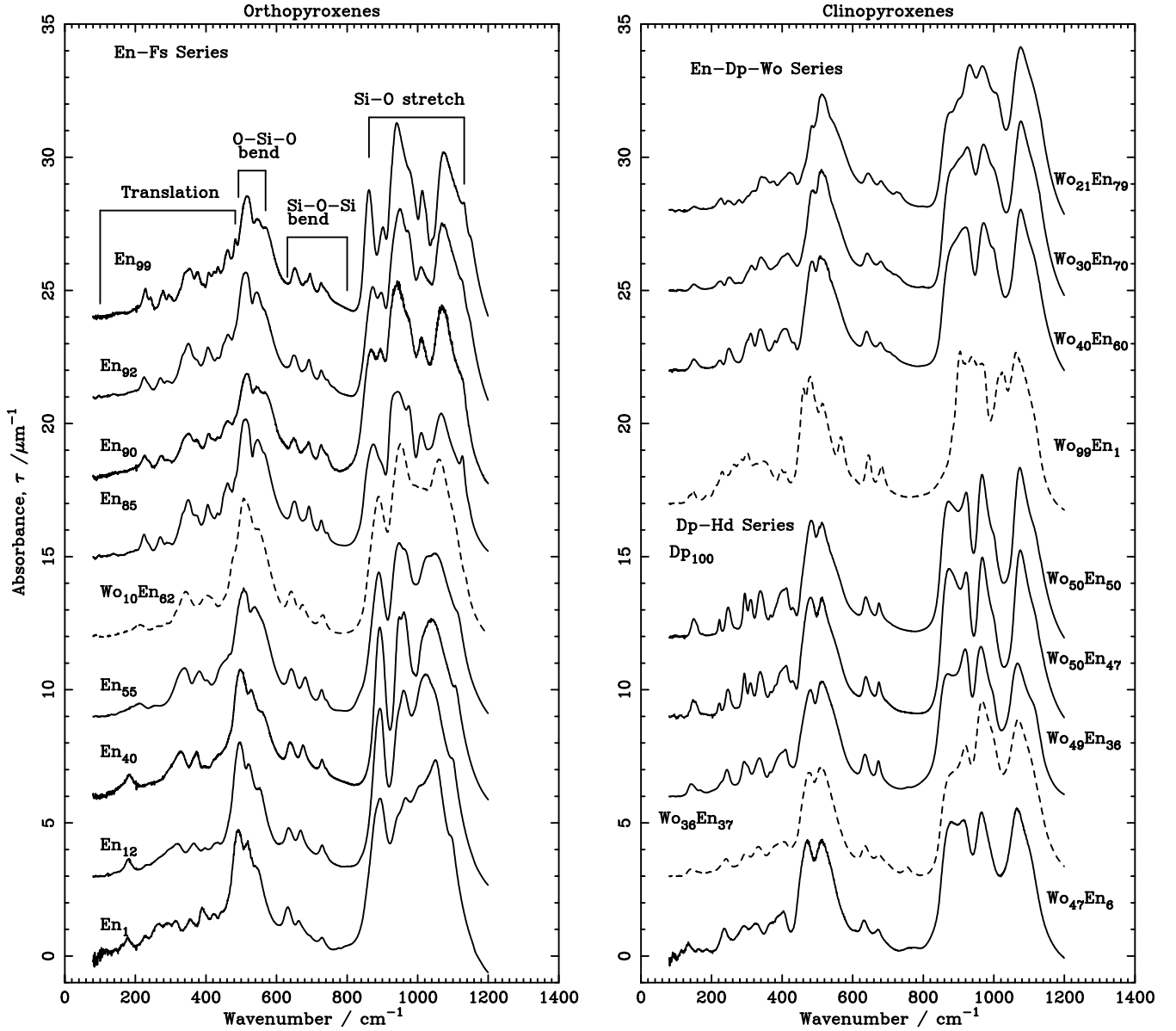


Figure 4. Left: Orthopyroxenes in the Enstatite-Ferrosilite solid-solution series, each spectrum is offset by 3 from the spectrum below it. The spectrum of pigeonite, $Wo_{10}En_{62}$ resembles an En-Fs pyroxene even though it is of intermediate composition (dashed curve). Right: Clinopyroxenes in the Enstatite-Diopside-Wollastonite and Diopside-Hedenbergite solid-solution series. Spectra of the end-member *pyroxenoid* wollastonite, Wo_{99} and the Dp-Hd-like spectrum of pigeonite $Wo_{36}En_{37}$ are dashed because their compositions are not on the edges of the pyroxene quadrilateral. Clinopyroxene offsets from the bottom are: Dp-Hd: 0, 3, 6, 9, 12; En-Dp-Wo: 17, 22, 25, 28.

in the spectra due to temperature and those due to changes in chemical composition. Since each band arises from part of the crystal structure (e.g. the Si-O-Si bend or translations of the position of the cations relative to the tetrahedra) there will be ambiguity between different silicates, and between silicates and other solids containing similar bonds. An analogy would be to consider the spectral signature of rings of carbon atoms in organic molecules: a spectral feature is indicative of a part of a molecule, not the entire structure.

Changes in the Si-O stretching, Si-O-Si bending and O-Si-O-bending modes with composition are presented in Figure 5 and the bands listed in Tables 2 and 3; changes in the Translations are examined in Figures 5 and 6 and the

bands listed in Tables 3 and 4. The fitted compositional-dependence of the peak wavelengths of prominent bands are listed in Table 5. Stronger and distinctive bands are labelled according to their likely carriers: *S*, Si-O stretch, *SiB*, Si-O-Si bend, *OS*, O-Si-O bend, *T*, translation. Letters in front of the carrier assignment indicate the pyroxene series *s*, orthopyroxenes (En-Fs series), *c*, clinopyroxenes, *h*, Dp-Hd series, *w*, En-Dp-Wo series, *a*, all pyroxenes studied; the letter *w* after a band name indicates a weak band. Some bands of the En-Fs series have different compositional wavelength shifts at either end of the series, bands at the Mg-rich end ($En \gtrsim 50$ per cent) are denoted by the subscript *E*, Fe-rich bands at the Fe-rich end ($En \lesssim 50$ per cent) are labeled *F*.

Numerical subscripts increase with increasing wavelength. In the sections below wavelengths in parentheses are the wavelength of the pyroxene with the highest Mg content. Due to the complexity of the pyroxene spectra, band positions were determined by close inspection of the frequency-based spectra; a fuller treatment of band shapes is beyond the scope of this paper, but will be presented together with the structural constraints on a later paper in the mineralogical literature.

5.1 Bands common to all studied pyroxenes

Only two narrow bands are common to all the pyroxenes (Figure 5, and Tables 2, 3 and 5) an Si–O stretching mode, *aS*, (10.22 μm ; En_{99}) and an Si–O–Si-bending mode, *aSiB* (15.34 μm ; En_{99}). *aS* shifts by only 0.15 μm as Mg is replaced; the band is indistinct in the orthopyroxenes, due to the dominance of a neighbouring blended band (*oS_{2E}*), but becomes more prominent in the clinopyroxenes when Ca increases from 20–50 percent, and strongest for diopsides ($\approx \text{Wo}_{50}\text{En}_{50}\text{Fs}_{50}$). In contrast, the common bending-mode, *aSiB*, is prominent across our range of pyroxene samples and shifts by only 0.51 μm to 15.85 μm in En_1 .

5.2 Si–O stretches

The orthopyroxene bands (Figure 5(a)+(g), Tables 2 and 5) are: *oS₁*, (9.32 μm ; En_{99}), *oS_{2E}* (10.64 μm ; En_{99}) and *oS₃* (11.60 μm ; En_{99}) which is subdivided into two components, *oS_{3E}* and *oS_{3F}*. Increases in the proportion of Fe reduce the overall width of the whole stretching feature due to the shift of *oS₁* by +0.47 μm and the decrease in the wavelength of band *oS_{3E}* from 11.60 μm (En_{99}) to 11.20 μm (En_{40}). In contrast, band *oS_{3F}* remains at 11.2 μm does not shift in wavelength between En_{40} and En_1 . Both the wavelength and width of the band resemble those of peaks seen in many astronomical sources in which the carrier is frequently identified as olivine (e.g. in comets Hanner, Lynch & Russell 1994) or occasionally as a polyaromatic-hydrocarbon absorption feature (Bregman et al. 2000). It could also contribute to the shoulder identified as olivine Mg-end-member forsterite (e.g. Do-Duy et al. 2020) in young stellar objects and the ISM. The 10.64–10.55- μm *oS_{2E}* band shifts by only +0.1 μm between En_{99} and En_{40} and probably merges with *aS* at $\text{En} \sim 12$ per cent.

The characteristic Si–O-stretching bands of Ca-bearing clinopyroxenes (Figure 5(d)+(g), Tables 2 and 5) are: *aS* and *cS* (9.29 μm ; $\text{Wo}_{21}\text{En}_{79}$). In addition, the En – Dp series has band *wS* (10.74 μm ; En_{79} – En_{40}) which shifts by +0.15 μm and the Dp – Hd series, *hS* (10.86 μm ; En_{50} – En_6) shifts by only +0.08 μm across the series. Clinopyroxenes with diopside-like compositions ($\text{Wo}_{30}\text{En}_{70}$ to $\text{Wo}_{49}\text{En}_{36}$) have a prominent shoulder, *dS* at 11.43–11.55 μm . In common with the orthopyroxenes, the width of the overall Dp – Hd series Si–O stretching region becomes narrower with increasing Fe content.

Wavelength shifts of *aS*, *cS* and *hS* have a similar dependence on the percentage of Mg $\sim 0.002 \times x$, where x is the percentage of Mg (Figure 5(g), Table 5).

5.3 Si–O–Si bend

These modes are produced in the linkages between SiO_4 tetrahedra; we observed three prominent bands in orthopyroxenes (Figure 5 (b)+(h)), but only two bands in clinopyroxenes (Figure 5(e)+(h)); Tables 3 and 5. The three orthopyroxene-bands are *aSiB* (15.34 μm ; En_{99}), *oS_{1B}* (13.77 μm ; En_{99}) and *oS_{2B}* (14.39 μm ; En_{99}); there is also a weak band *oS_{1B_w}* (13.46 μm ; En_{99}) in En_{99} to En_{12} . *oS_{1B_w}* and *oS_{1B}* barely shift with composition (≤ 0.04 μm) but *oS_{2B}* shifts by 0.69 μm . The clinopyroxenes and pyroxenoid have two Si–O–Si bands: *aSiB* and *cSiB* (14.71 μm in $\text{Wo}_{21}\text{En}_{79}$); *cSiB* shifts by 0.17 μm across the range to $\text{Wo}_{47}\text{En}_6$.

The Si–O–Si bending-modes might be the most promising region for the identification of chain silicates in the 5–28- μm spectral-range of the *Mid-Infrared Instrument (MIRI)* on the *James Webb Space Telescope (JWST)* because the spectra of other silicate groups previously studied by us are quite different between 12 and 16 μm : olivines do not display these bands due to the absence of tetrahedral linkages (e.g. Hofmeister & Pitman 2007) and of the hydrous silicates, talc has only one narrow band at 14.92 μm which might overlap with some of the diopsides, and amphiboles have only a single band at 13.15 μm (Hofmeister & Bowey 2006); silicas (SiO_2 minerals) have narrow bands at 12.5–12.8 μm , 14.4–14.6 μm (Koike et al. 2013) which are different from the pyroxene bands.

5.4 O–Si–O bends

For this motion, orthopyroxenes have three narrow bands, whereas clinopyroxenes have two broader bands.

The orthopyroxene bands (Figure 5(c)+(i), Tables 3 and 5) are: *oOB₁* (17.54 μm ; En_{99}) which shifts by 0.81 μm between En_{99} and En_1 and *oOB₂* (18.28 μm ; En_{99}) and *oOB₃* (19.42 μm ; En_{99}) which both shift by 0.99 μm . The behaviour of the clinopyroxene bands (Figure 5(f)+(i), Tables 3 and 5) is different: the common *cOB* band (19.49 μm ; $\text{Wo}_{21}\text{En}_{79}$) does not shift significantly with composition, the Dp – Hd -band, *hOB* (20.75 μm ; Dp_{100}) shifts by 0.48 μm across the range En_{50} – En_6 whilst the En – Dp -band *wOB* decreases in wavelength by 0.44 μm as Ca replaces Mg (En_{79} to En_{60}). The non-shifting *cOB*-band overlaps *oOB₃* above En_{99} : so a similarly-shaped feature at 20.0–20.4 μm could indicate an orthopyroxene with $\text{En} \lesssim 60$ per cent.

5.5 Translations

Translational bands exhibit the largest wavelength shifts with composition because cations are less tightly bound than are the chains of SiO_4 tetrahedra. Two orthopyroxene translations (Figures 5(c),(f),(i) and 6(a),(b),(e),(f)) have small shifts in the En_{99} – En_{55} -range: *oT_{1E}* (21.74 μm ; En_{99}) decreases in wavelength by 0.23 μm , while and *oT_{3E}* (26.60 μm ; En_{99}) moves by +0.14 μm . In contrast, bands *oT₂* (24.57 μm ; En_{99}) and *oT₄* (28.25 μm ; En_{99}) each shift by ~ 3.5 μm across the En_{99} – En_1 -range. *oT₅* (35.84 μm ; En_{99}) has the largest shift of any pyroxene band: 8.02 μm En_{99} – En_1 . Chihara et al. found the largest shift was for a band at 43 μm in En_{100} which moved to 56 μm in En_0 . With our wider

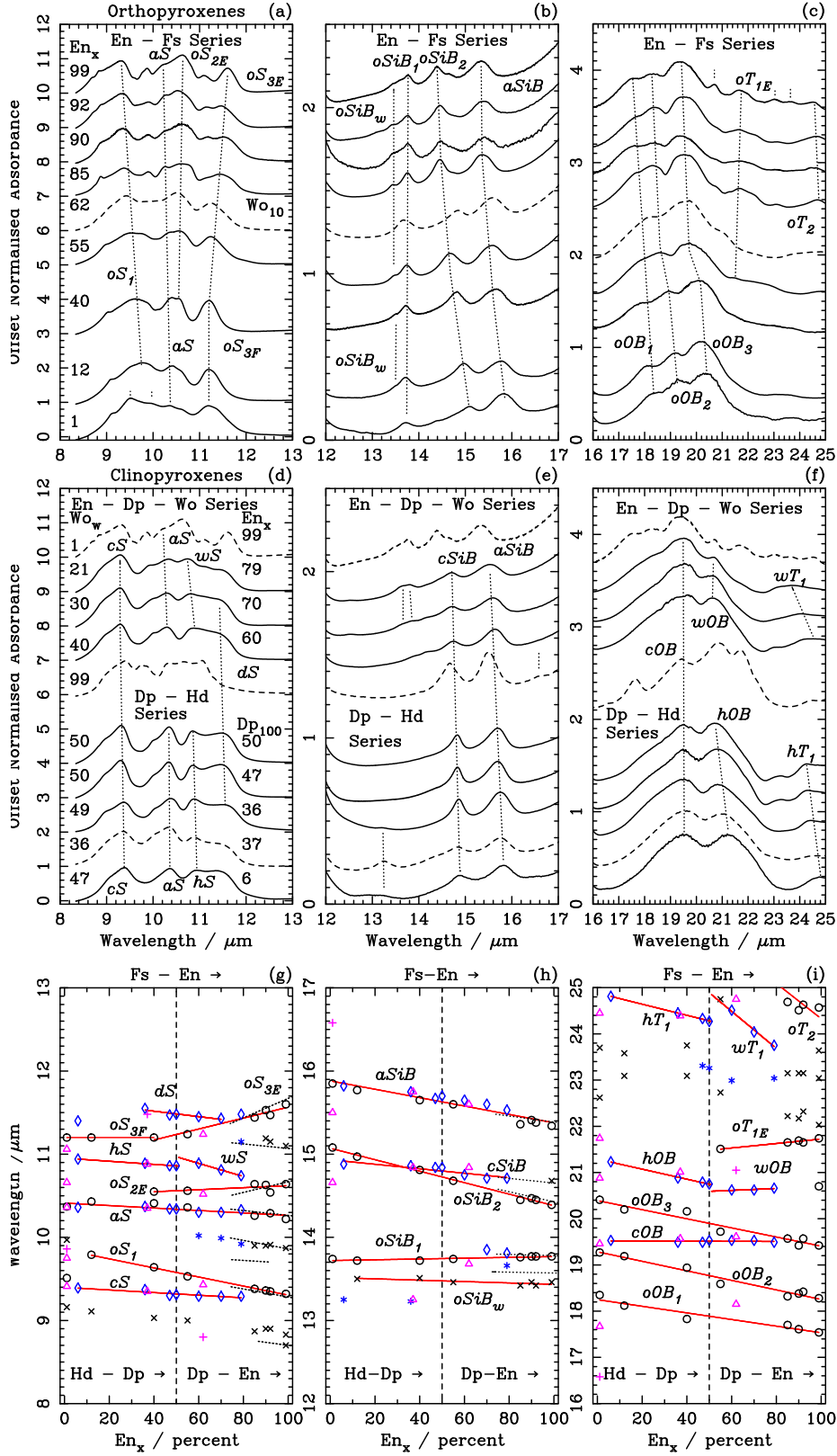


Figure 5. Left to Right: Detail in the Si-O stretching, Si-O-Si bending modes, O-Si-O bending modes and the highest frequency translations of ortho- and clinopyroxenes. Bottom Row: Peak positions as a function of Mg content: solid red lines are fits to the strongest peak shifts, black dotted lines are fits to the peak shifts in meteoritic spectra obtained by [Bowey et al. \(2007\)](#). Open symbols indicate prominent bands: En-Fs orthopyroxenes – black \circ , \times ; En-Dp and Dp-Hd clinopyroxenes – blue \diamond , * and pigeonites and wollastonite – magenta Δ ,

Table 2. Si–O stretch - peak wavelengths of bands. Pigeonites of intermediate composition and bands not used in fitting are indicated with bracketed italics. Bands with large compositional wavelength shifts are indicated in bold. Scatter in the measurements indicates an uncertainty of $\pm 0.015\mu\text{m}$

Sample	Band assignment and measured wavelength (μm)										
En99	8.70	8.83	9.32	9.87	10.22	10.64	11.10	11.60			
En92		8.90	9.35	9.91	10.29	10.54	11.15	11.47			
En90		8.90	9.36	9.90		10.63	11.19	11.53			
En85		8.87	9.38	9.90	10.26	10.64		11.44			
(<i>Wo</i> ₁₀ <i>En</i> ₆₂)		(<i>8.80</i>)	(<i>9.43</i>)			(<i>10.52</i>)		(<i>11.24</i>)			
En55		9.00	9.53		10.36	10.56		11.24			
								<i>oS_{3F}</i>			
En40		9.03	9.64		10.41	10.55		11.20			
En12		9.11	9.79		10.43			11.20			
En1		9.16		9.51	9.97	10.37		11.20			
			<i>cS</i>				<i>wS</i>	<i>dS</i>			
Wo ₂₁ En ₇₉			9.29	9.92	10.33	10.74	11.15	(<i>11.48</i>)			
Wo ₃₀ En ₇₀			9.29	9.99	10.30	10.81		11.43			
Wo ₄₀ En ₆₀			9.29	10.02	10.30	10.89		11.45			
								<i>hS</i>			
Wo ₅₀ En ₅₀			9.31		10.34	10.86		11.48			
Wo ₅₀ En ₄₇			9.30		10.34	10.86		11.47			
(<i>Wo</i> ₃₆ <i>En</i> ₃₇)			(<i>9.35</i>)		(<i>10.35</i>)	(<i>10.88</i>)		(<i>11.48</i>)			
Wo ₄₉ En ₃₆			9.37		10.37	10.89		11.55			
Wo ₄₇ En ₆			9.39		10.36	10.94		(<i>11.40</i>)			
Pyroxenoid (no band assignments)											
Wo ₉₉			9.41	9.75	9.86	10.36	10.66	11.06			

Table 3. O–Si–O, Si–O–Si Bends and the highest frequency orthopyroxene translation, uncertainty in wavelength $\sim \pm 0.02\mu\text{m}$ near $13\mu\text{m}$ and $\sim \pm 0.04\mu\text{m}$ at $20\mu\text{m}$

Sample	Band assignment and peak wavelength (μm)										
En99	<i>oS_{iB_w}</i>	<i>oS_{iB₁}</i>	<i>oS_{iB₂}</i>	<i>aSiB</i>	<i>oOB₁</i>	<i>oOB₂</i>	<i>oOB₃</i>	<i>oT_{1E}</i>			
En99	13.46	13.77	14.39	14.68	15.34	17.54	18.28	19.42	20.70	21.74	23.04
En92	13.42	13.77	14.45		15.38		18.42	19.57		21.65	23.15
En90	13.46	13.77	14.47		15.41	17.61	18.38	19.42		21.69	23.15
En85	13.42	13.76	14.45		15.36	17.70	18.32	19.57		21.65	23.15
(<i>Wo</i> ₁₀ <i>En</i> ₆₂)		(<i>13.68</i>)	(<i>14.84</i>)		(<i>15.60</i>)		(<i>18.15</i>)	(<i>19.61</i>)		(<i>21.05</i>)	
En55	13.46	13.74	14.68		15.60		18.59	19.72		21.51	
En40	13.51	13.72	14.81		15.65	17.83	18.94	20.16			23.09
En12	13.50	13.72	14.97		15.77	18.12	19.19	20.20			23.09
En1		13.74	15.08		15.85	18.35	19.27	20.41			22.62
				<i>cSiB</i>				<i>cOB</i>	<i>wOB</i>		
Wo ₂₁ En ₇₉	13.66	13.81		14.71	15.53			19.49	20.66		23.04
Wo ₃₀ En ₇₀		13.85		14.71	15.60			19.53	20.62		
Wo ₄₀ En ₆₀				14.75	15.65			19.53	20.62		
								<i>hOB</i>			
Wo ₅₀ En ₅₀				14.84	15.70			19.53	20.75		23.26
Wo ₅₀ En ₄₇				14.84	15.67			19.49	20.79		
Wo ₄₉ En ₃₆	13.23			14.86	15.75			19.49	20.88		
(<i>Wo</i> ₃₆ <i>En</i> ₃₇)	(<i>13.25</i>)			(<i>14.84</i>)	(<i>15.75</i>)			(<i>19.57</i>)	(<i>21.01</i>)		
Wo ₄₇ En ₆	13.25			14.88	15.82			19.53	21.23		
Pyroxenoid bands (no band assignments)											
Wo ₉₉				14.66	15.50	16.58	17.67	19.46	20.88	21.74	

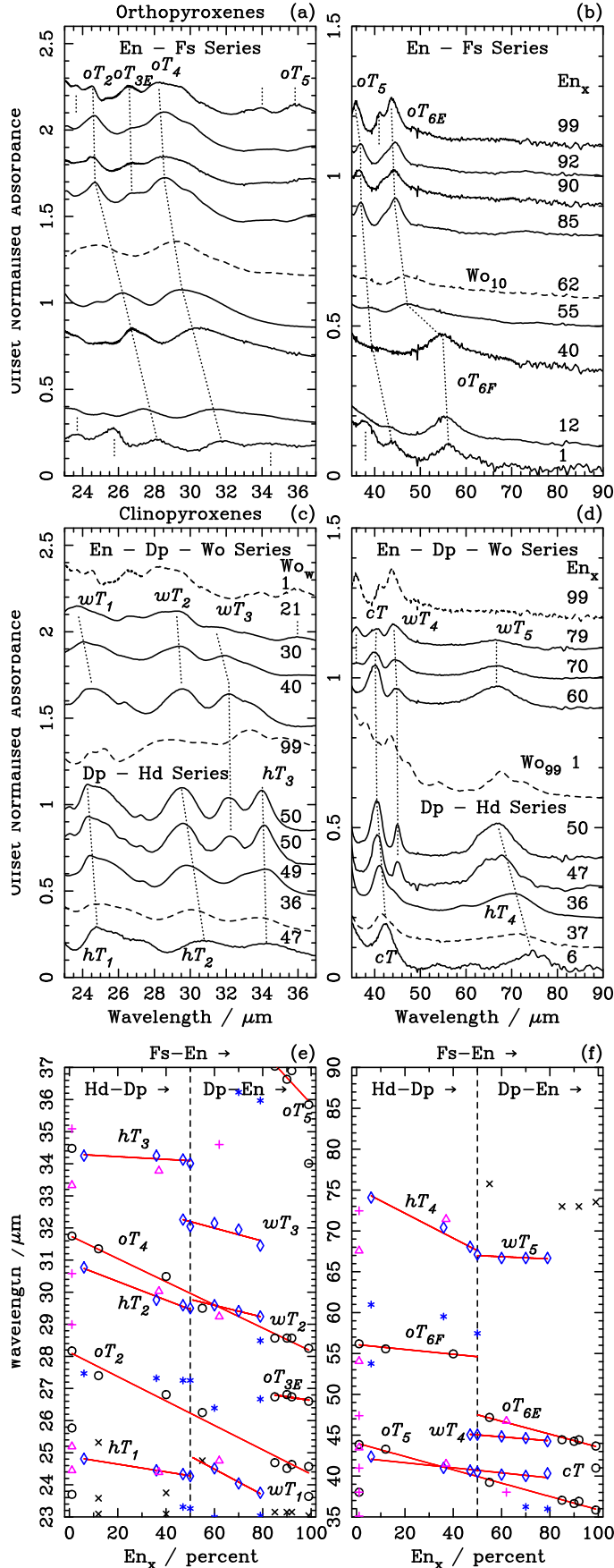


Figure 6. Detail in the Translational bands. Bottom Row: Peak positions as a function of Mg content. See Figure 5 for key to plotting symbols.

Table 4. Translations. Uncertainty at 20 μm ± 0.04 , for the broad clinopyroxene 60 μm peak is $\pm 0.5 \mu\text{m}$. The orthopyroxene peaks above 70 μm are ill-defined in our data (see Section 6.2)

Sample		Band assignment and peak wavelength (μm)									
		<i>oT</i>₂	<i>oT</i> _{3E}	<i>oT</i>₄			<i>oT</i>₅		<i>oT</i>_{6E}	?	
En ₉₉	23.64	24.57	26.60	28.25	29.50	34.01 ^a	35.84	40.98	43.67	73.5	
En ₉₂		24.63	26.74	28.57	30.12		36.90		44.44	73.0	
En ₉₀		24.51	26.81	28.57			36.63		44.25		
En ₈₅		24.69	26.74	28.57	30.03		37.04		44.44	73.0	
(<i>Wo</i> ₁₀ <i>En</i> ₆₂)		(24.75)		(29.24)			(38.02)		(46.73)		
En ₅₅	24.75	26.25		29.50			39.22		47.17		
									<i>oT</i>_{6F}		
En ₄₀	23.75	26.81		30.49					54.95	75.8	
En ₁₂	23.58	25.32	27.40	31.35			43.29		55.56		
En ₁	23.70	25.77	28.17	31.75		34.48	38.02	43.86	56.18		
		<i>wT</i> ₁			<i>wT</i> ₂	<i>wT</i> ₃		<i>cT</i>	<i>wT</i> ₄	<i>wT</i> ₅	
Wo ₂₁ En ₇₉	23.75			26.67	28.49	29.24	31.45	35.97	40.32	44.25	
Wo ₃₀ En ₇₀	24.04					29.41	31.95		40.00	44.64	
Wo ₄₀ En ₆₀	24.51		26.39			29.59	32.15		40.16	44.84	
		<i>hT</i>₁		<i>hT</i>₂		<i>hT</i> ₃				<i>hT</i>₄	
Wo ₅₀ En ₅₀	24.27			27.25	29.50	32.05	34.01		40.49	45.05	
Wo ₅₀ En ₄₇	24.33			27.25	29.59	32.26	34.13		40.65	45.05	
Wo ₄₉ En ₃₆	24.45			27.32	29.76		34.25		40.98	70.4	
(<i>Wo</i> ₃₆ <i>En</i> ₃₇)	(24.39)	(25.19)	(26.53)		(30.03)		(33.78)		(41.49)	(71.43)	
Wo ₄₇ En ₆	24.81			27.47	30.77		34.25		42.37	74.1	
Pyroxenoid bands (no band assignments)											
Wo ₉₉	24.45	25.19		28.99	33.33	35.09	38.02	43.48		47.39	
									54.05	67.6	
										72.5	

^a merged with weak band at 33.11, very broad weak peaks are seen in other members of the group

range of orthopyroxenes, we find that this band has two disjointed components: *oT*_{6E} which shifts from 43.7 μm (En₉₉) to 47.2 μm (En₅₅) and *oT*_{6F} which occurs at 55.0 μm (En₄₀) and 56.2 μm (En₁) giving a combined shift of 12.5 μm .

The clinopyroxene-series' (Figure 6(c),(d)) have only one common translation, *cT*, (40.32 μm ; Wo₂₁En₇₉) which shifts by 2.05 μm across the En₇₉–En₆ range. The shifts of En–Dp pyroxenes are relatively small: *wT*₁ (23.75 μm ; Wo₂₁En₇₉) and *wT*₂ (29.24 μm ; Wo₂₁En₇₉) shift in the En₇₉–En₆₀ range, by 0.76 and 0.35 μm , respectively. *wT*₂ shifts in parallel with *wT*₃ (31.45 μm ; Wo₂₁En₇₉) and *wT*₄ (44.25 μm ; Wo₂₁En₇₉) which vary by $\sim 0.002 \times x$ down to $x = 47$. *wT*₅ (66.7 μm) is the broadest band measured ($\sim 10\mu\text{m}$), but shifts by only 0.44 μm despite its long peak-wavelength.

In common with the orthopyroxenes, Dp–Hd clinopyroxenes show much more variable shifts: *hT*₁ (24.27 μm ; Dp₁₀₀) and *hT*₃ (34.01 μm ; Dp₁₀₀) shift by 0.54 and 0.24 μm , respectively *hT*₂ (29.5 μm ; Dp₁₀₀) has a similar slope to *cT*, and the total shift is 1.27 μm . However, the most striking difference in the clinopyroxene shifts is that in contrast to the *wT*₅ band of En–Dp clinopyroxenes, the broadest and lowest frequency band of the Dp–Hd series *hT*₄ (67.1 μm ; Dp₁₀₀) has a large wavelength shift of 7.0 μm between En₅₀ and En₆.

6 LIMITATIONS IN OUR DATA SET

6.1 Undetectable effect of clinopyroxene on En₉₉

Hofmeister (2012) found that the meteoritic sample from which En₉₉ is derived contains 5 per cent of microscopic inclusions (blebs) of composition $\text{Mg}_{1.10}\text{Ca}_{0.85}\text{Na}_{0.02}\text{Al}_{0.02}\text{Si}_2\text{O}_6 \equiv \text{Wo}_{43}\text{En}_{55}$, a level, just above canonical detection limit in infrared spectra. Unfortunately we do not have a spectrum of Wo₄₃En₅₅ to compare with our data and we do not know if the thin film made from sample was similarly contaminated. The spectrum of En₉₉ contains extra peaks that do not appear in the rest of the En–Fs orthopyroxene series. However, this could be because it is of end-member composition. Bands which look like clinopyroxene peaks are a shoulder at 14.68 μm (*cSiB*), and fairly prominent peaks at 20.70 μm (*wOB* / *hOB*), 34.01 μm (*hT*₃) and 40.98 μm (*cT*). These features were also identified by Chihara et al. in their magnesium-rich synthetic samples which contained no Wo₄₃En₅₅, therefore we consider these bands intrinsic to En₉₉ and not the result of contamination.

6.2 Unobserved bands above 70 μm

Bowey et al. (2001) detected a weak pair of bands in En₈₅ centred at 71.01 μm and 73.83 μm at room temperature which are not properly distinguishable from the noise in the current data. There are hints of structure near 73 μm in En₉₉, En₉₂, En₈₅ and at 75.8 μm in En₅₅. The most likely

Table 5. Dependence of the peak positions of stronger and distinctive bands on the proportion of Mg in the pyroxenes. Bands with the largest wavelength shifts are highlighted in bold, those with negligible wavelength shifts, or small wavelength shifts with low Pearson correlation coefficients $|R^2| < 0.7$ are italicised.

Series	Label ^a	λ <i>En_{max}</i>	Range per cent	$\Delta\lambda^b$ μm	Fit $\text{En}_0 + b\text{En}_x$	$ R^2 $
Si–O stretch						
All	<i>aS</i>	10.22	99– 1	0.15	10.412 – 0.0015	0.8
En–Fs	<i>oS₁</i>	9.32	99–12	0.47	9.850 – 0.0055	1
	<i>oS_{2E}</i>	<i>10.64</i>	<i>99–40</i>	<i>0.09</i>	<i>10.500 + 0.0012</i>	<i>0.6</i>
	<i>oS_{3E}</i>	11.60	99–40	–0.40	10.908 + 0.0066	1
	<i>oS_{3F}</i>	<i>11.20</i>	<i>40– 1</i>	<i>0.00</i>	<i>11.20</i>	–
Clino	<i>cS</i>	9.29	79– 6	0.10	9.398 – 0.0016	0.9
	<i>dS</i>	11.43	70–36	0.12	11.648 – 0.0033	0.9
En–Wo	<i>wS</i>	10.74	79–40	0.15	11.364 – 0.0079	1
Dp–Hd	<i>hS</i>	10.86	50– 6	0.08	10.952 – 0.0019	1
Si–O–Si bend						
All	<i>aSiB</i>	15.34	99– 1	0.51	15.882 – 0.0050	0.9
En–Fs	<i>oS_{iB_w}</i>	<i>13.46</i>	<i>99–12</i>	<i>0.04</i>	<i>13.517 – 0.0008</i>	<i>0.8</i>
	<i>oS_{iB_l}</i>	<i>13.77</i>	<i>99– 1</i>	<i>–0.03</i>	<i>13.720 + 0.0005</i>	<i>0.9</i>
	<i>oS_{iB₂}</i>	14.39	99– 1	0.69	15.072 – 0.0069	1
Clino	<i>cSiB</i>	14.71	79– 6	0.17	14.933 – 0.0027	0.9
O–Si–O bend						
En–Fs	<i>oOB₁</i>	17.54	99– 1	0.81	18.249 – 0.0072	1
	<i>oOB₂</i>	18.28	99– 1	0.99	19.285 – 0.010	1
	<i>oOB₃</i>	19.42	99– 1	0.99	20.393 – 0.0099	1
Clino-	<i>cOB</i>	<i>19.49</i>	<i>79– 6</i>	<i>0.04</i>	<i>19.520 – 0.0001</i>	<i>0.2</i>
En–Wo	<i>wOB</i>	20.66	79–60	–0.04	20.489 + 0.0021	0.9
Dp–Hd	<i>hOB</i>	20.75	50– 6	0.48	21.290 – 0.011	1
Translations						
En–Fs	<i>oT_{1E}</i>	21.74	99–55	–0.23	21.240 + 0.0048	1
	<i>oT₂</i>	24.57	99– 1	3.60	28.130 – 0.038	1
	<i>oT_{3E}</i>	26.60	99–85	0.14	27.769 – 0.011	0.8
	<i>oT₄</i>	28.25	99– 1	3.50	31.766 – 0.036	1
	<i>oT₅</i>	35.84	99– 1	8.02	44.027 – 0.082	1
	<i>oT_{6E}</i>	43.67	99–55	3.50	51.45 – 0.079	1
	<i>oT_{6F}</i>	55.0	40– 1	1.23	56.09 – 0.03	1
clino-	<i>cT</i>	40.32	79– 6	2.05	42.25 – 0.031	0.9
En–Wo	<i>wT₁</i>	23.75	79–60	0.76	26.896 – 0.040	1
	<i>wT₂</i>	29.24	79–60	0.35	30.696 – 0.018	1
	<i>wT₃</i>	31.45	79–47	0.81	33.213 – 0.020	0.9
	<i>wT₄</i>	44.25	79–47	0.78	46.26 – 0.024	1
	<i>wT₅</i>	66.7	79–50	0.44	67.67 – 0.01	0.8
Dp–Hd	<i>hT₁</i>	24.27	50– 6	0.54	24.883 – 0.012	1
	<i>hT₂</i>	29.50	50– 6	1.27	30.912 – 0.029	1
	<i>hT₃</i>	34.01	50– 6	0.24	34.307 – 0.0042	0.7
	<i>hT₄</i>	67.1	50– 6	7.0	75.20 – 0.2	1

^a Bands are labelled according to their likely carriers: *S*, Si–O stretch, *SiB*, Si–O–Si bend, *OS*, O–Si–O bend, *T*, translation. Letters in front of the carrier assignment indicate the pyroxene series *o*, orthopyroxenes (En–Fs series), *c*, clinopyroxenes, *h*, Dp–Hd series, *w*, En–Dp–Wo series, *a*, all pyroxenes studied; the letter *w* after a band name indicates a weak band. Some bands of the En–Fs series have different compositional wavelength shifts at the En and Fs ends of the series, bands at the Mg-rich-end (En \gtrsim 50 per cent) are denoted by the additional subscript *E*, bands at the Fe-rich end (En \lesssim 40 per cent) are denoted with *F*. Numerical subscripts increase with increasing wavelength.

^b $\Delta\lambda = \lambda(\text{En}_{\text{max}}) - \lambda(\text{En}_{\text{min}})$, where En_{max} and En_{min} are the maximum and minimum per cent fractions, respectively.

cause of their absence is an insufficiently thick film and low detector signal-to-noise ratios. It would be particularly useful to fully-explore this spectral range because Chihara et al. measured differences between clino- and orthoenstatite at longer wavelengths, namely a pairs of bands at 49.2 μm and

51.6 μm , and 68.7 μm and 72.5 μm in orthoenstatite (Oen; *oEn*₁₀₀) which were not observed in clinoenstatite (Cen; *cEn*₁₀₀); clinoenstatite had a narrow band at 65.9 μm . The Cen and Oen spectra were identical at wavelengths \lesssim 40 μm .

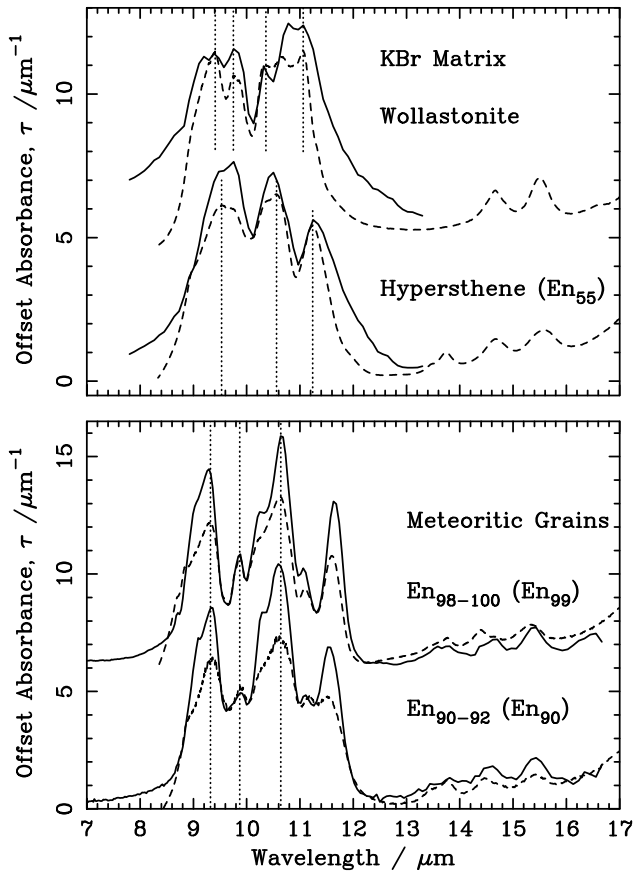


Figure 7. Comparison of DAC spectra (dashed curves) with Ferraro KBr-pellet-spectra (solid curves) and with those of individual crushed meteoritic grains (solid curves) obtained in a Diamond Compression Cell (Bowey et al. 2007). The ratios between strong and weak peaks change as does the spectral contrast, but the features are not wavelength-shifted provided the minerals have similar chemical compositions.

The longest band they identified was a peak at 86.1 μm in En_0 .

7 CONSISTENCY OF ROOM-TEMPERATURE AND LOW-TEMPERATURE PARTICULATE SPECTRA

7.1 Comparison with room temperature data obtained with KBr and polyethylene pellets

The DAC spectra are compared with published KBr-pellet spectra of similar terrestrial pyroxenes in Figures 7 and 8. The Ferraro spectra were obtained with the KBr-pellet technique (grain sizes are unknown, but small enough to produce consistent peaks) and digitized for comparison with low-resolution astronomical spectra (Bowey & Adamson 2002). The ratios between strong and weak peaks change as does the spectral contrast, but features are not wavelength-shifted provided the pyroxenes have similar chemical compositions. Spectra obtained with the KBr technique have recognisably similar shapes to the DAC spectra and the peaks are not wavelength-shifted. The KBr spectra are broader than our

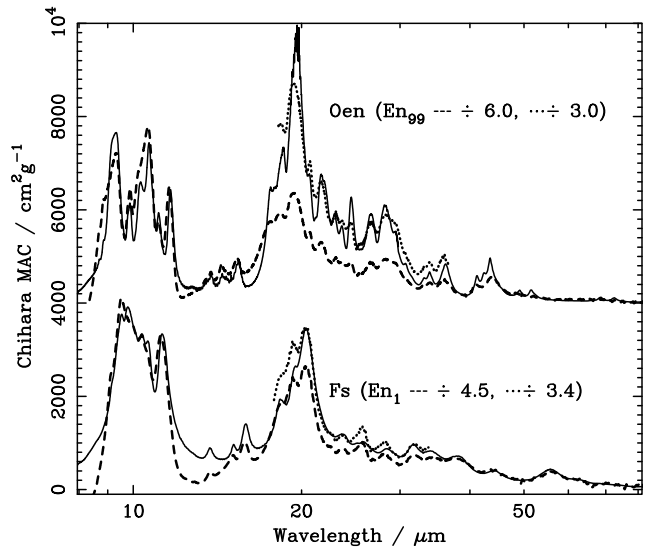


Figure 8. Comparison with Chihara et al. KBr and polyethylene pellet data (solid curves) for synthetic orthoenstatite ($\text{Oen} \equiv \text{En}_{100}$) and ferrosilite ($\text{Fs} \equiv \text{En}_0$). Other curves are our data for En_{99} and En_1 samples converted to mass absorption coefficients scaled to match features in their data.

data due to the scattering of light at boundaries between the grains and the matrix. If differences in refractive index are substantial at grain boundaries some light will be reflected back along its path as it passes into the grain and again as it passes back into the KBr. It is difficult to control particle density and clumping in a KBr dispersion: if these parameters are too large the measured bandwidths will increase due to the increased scattering, even if the majority of grains are sufficiently small. In the DAC the only substantial change in refractive index occurs at the surface of the diamonds, and its effect is mitigated by subtracting the spectrum of the empty cell from the data.

KBr- and polyethylene-pellet spectra of synthetic MgSiO_3 (Oen) and FeSiO_3 (Fs) orthopyroxenes obtained by Chihara et al., are compared with our En_{99} and En_1 samples in Figure 8. The peak wavelengths quoted by Chihara et al. are consistent with our data. However, there is a substantial difference in our derived mass absorption coefficients. Their mass absorption coefficients are factors of 6.0 (En_{99}) and 4.5 (En_1) weaker than ours in the Si–O stretching and Si–O–Si bending regions (8–17 μm) and in the far-infrared beyond $\sim 40 \mu\text{m}$, but the discrepancy in the 17–40 μm range for En_{99} is a factor of 3.0 and 3.4. Some large individual bands are much sharper than ours which is possibly an effect of the DAC spectra not fully-sampling the c-axis due to the lath-like pyroxenes lying on their sides when crushed. These discrepancies occur because infrared spectra depend on the distance photons travel between grain-scattering and absorption events but the scattering measurement is complicated by the close correlation of absorption and reflection when the bands are strong. For this reason, different size grains are sampled by light transmitted by different motions within the crystal. DAC and Diamond-Compression-Cell (DCC) measurements (see Section 7.2, below) reduce the effect of scattering because abutted grains have very sim-

ilar refraction indices so that the reflection at grain boundaries is minimized and the absence of scattering enhances the observed mass absorption coefficients.

We also suspect that some of the Chihara et al. spectra contain small proportions of quartz (SiO_2) in addition to the olivine they identified because their data show peaks at $12.5 \mu\text{m}$ and $14.4 \mu\text{m}$ and enhanced absorption at $9.2 \mu\text{m}$. The effect of these impurities could be subtracted by the method used in Appendix A1. None of these issues invalidate their conclusions and their Oen and Fe spectra contain resolved peaks longward of $50 \mu\text{m}$, and $70 \mu\text{m}$, respectively, when ours do not.

7.2 Comparison with room temperature spectra of meteoritic grains

Meteoritic spectra were obtained by crushing individual micron-sized grains in a Diamond Compression Cell (Bowey et al. 2007); En_{98-100} is normalised average of 13 grains, En_{90-92} is the average spectrum of 3 grains. These spectra are not wavelength shifted in comparison with our spectra and the fitted compositional trends are similar (see Figure 5); where fits are different this is due to the much smaller compositional range covered by the meteoritic sample. Spectra of individual meteoritic grains have a much higher contrast in the strongest Si–O stretches than do the DAC spectra. Due to this higher contrast and the narrowness of the features in the tiny samples one or two extra, very weak, bands were observed in some of the meteoritic spectra.

7.3 Comparison with Room- and Low-Temperature Spectra

Both continuum, and spectral measurements of dust and ice indicate that the ambient temperature of dust in many astronomical environments (e.g. planetary nebulae, molecular clouds and the discs of young stellar objects) is much colder ($\sim 10\text{--}200 \text{ K}$) than the room temperature spectra obtained in most laboratory experiments. In order to explore the effect of temperature on the $17\text{--}85 \mu\text{m}$ spectra of crystalline olivines and pyroxenes Bowey et al. (2001) obtained measurements of powdered-samples mixed with petroleum jelly on 0.8-mm -thick polyethylene substrates at room- and low-temperature ($\sim 3.5 \text{ K}$). They found that 3.5-K peaks occurred at shorter wavelengths than do the corresponding 295-K peaks. In order to compare temperature-related wavelength shifts and compositional wavelength-shifts their data for pyroxenes are compared with our new spectra in Figure 9. As expected, wavelengths of bands and band shapes of their room-temperature spectra are consistent with our DAC spectra of samples from the same locality (i.e. samples with near identical compositions): our spectrum of En_{85} matches their spectrum of Bamble enstatite, as do $\text{Wo}_{50}\text{En}_{47}$ and the Bowey et al. (2001) diopside. However, the peak wavelengths of bands oT_{6E} and oT_4 in the 3.5 K spectra are best matched by our room-temperature En_{99} spectrum and oT_5 is best matched by En_{92} even though the low-temperature sample is En_{85} . If the low-temperature data were from an astronomical source, the conclusion could be that the enstatite is of near end-member, En_{100} , composition, i.e. it is 7 to 15 per cent richer in Mg than it really is, or that there

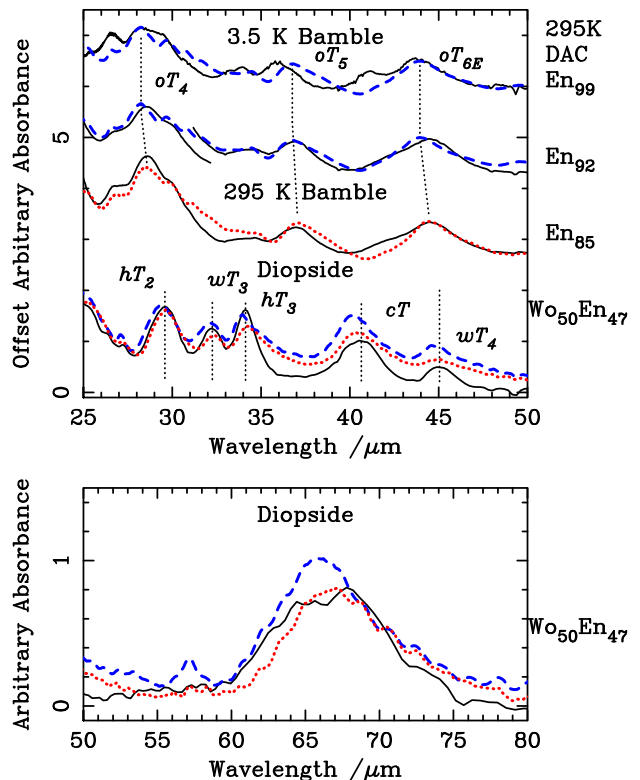


Figure 9. Comparison between room temperature DAC Enstatite and $\text{Wo}_{50}\text{En}_{47}$ spectra (solid) and *Bamble Enstatite* and *Diopside* room temperature (red dotted) and low temperature spectra (blue dashed) from Bowey et al. (2001). The matching DAC spectrum is indicated to the right of each spectrum. The difference in wavelength between room-temperature spectra of minerals of identical composition obtained by the two methods is insignificant within the uncertainties. However, the low temperature spectrum of En_{85} is blue-shifted with respect to the room temperature spectrum making it appear that the cold sample has the composition of room temperature En_{99} (bands oT_{6E} and oT_4), or En_{92} (oT_5), i.e. that it is 7–15% more Mg-rich than its known composition.

are two minerals contributing, En_{92} and En_{99} when only En_{85} is present.

There is less scope for temperature shifts to masquerade as compositional shifts in the diopside spectra because bands hT_2 , wT_3 and hT_3 only appear separately in near end-member diopsides in the Dp–Hd series and the temperature shifts are ten times greater ($0.1\text{--}0.3 \mu\text{m}$) than the available compositional shifts and cT is broader in the non-end-member clinopyroxenes. The longest wavelength band hT_4 is probably too broad and inspecific to pyroxenes to be useful for temperature studies; differences between the room-temperature spectra of this mineral are probably due to uncorrected fringes.

Low-temperature measurements of a wider-variety of pyroxenes are needed to properly quantify these effects, but the incorrect inferred compositional differences between our room-temperature and low-temperature laboratory spectra suggest that Mg-end-member astronomical enstatites identified in far-infrared astronomical spectra might not really be of end-member composition. A lower Mg:Fe ratio in the

astronomical dust would be more consistent with the ratios measured in the meteoritic enstatites sampled by [Bowey et al. \(2007\)](#).

8 SUMMARY

We present quantitative 8–90- μm spectra of 8 Mg- and Fe-bearing orthopyroxenes, 9 Mg-, Ca- and Fe-bearing clinopyroxenes and one Ca-bearing pyroxenoid obtained at room temperature. Spectra were obtained from thin films of finely-ground minerals crushed in a DAC without the use of an embedding medium. Pyroxenes have rich infrared spectra with many narrow peaks. In general, the wavelengths of the peaks increase as Mg is replaced in the lattice by Ca or Fe. However, two bands in the En-Fs (orthopyroxene) series shift to shorter wavelengths as the Fe component increases from 0 percent to 60 per cent. The most prominent band to do so is at 11.6 μm when Mg \sim 99 per cent and 11.2 μm when Mg \lesssim 40 per cent; below En₄₀ the band is more prominent and does not shift further with an increase in Fe. This 11.2 μm feature resembles an astronomical emission or absorption feature which is normally associated with olivines, forsterite or occasionally PAH absorption.

Only two bands are common to all the pyroxenes studied: an Si–O stretching mode at 10.22 μm in En₉₉ and an Si–O–Si-bending mode at 15.34 μm in En₉₉. We suggest that Si–O–Si bending modes between 13 and 16 μm hold promise for the identification of chain silicates in *MIRI* spectra obtained with the *JWST*, because the pyroxene pattern is distinct in this range.

The new spectra are compared with published 8–17 μm room-temperature transmission spectra of meteoritic pyroxenes and KBr- and polyethylene-pellet spectra of terrestrial pyroxenes. The ratios between strong and weak peaks change as does the spectral contrast, but the 10- μm features are not wavelength-shifted provided the minerals have the same chemical composition and crystal structure. However, because scattering between grain boundaries is reduced in DAC measurements of compressed powders, mass absorption coefficients in our data are up to 6 times the values measured in KBr and polyethylene pellets.

Room-temperature data from a [Bowey et al. \(2001\)](#) 17–85 μm study of two of our samples embedded in petroleum jelly on polyethylene substrates have band-shapes, wavelengths and relative-band-strengths which are consistent with our DAC spectra. However, comparison of their low-temperature spectra with our room-temperature data indicates that the spectroscopically identified ‘Mg-end-member’ grains in 10 K astronomical dust might contain 8–15 percent Fe due to temperature-related wavelength shifts to the blue at low temperatures masquerading as compositional shifts in peak wavelength. Low- and intermediate-temperature far-infrared measurements of a wider-variety of pyroxenes and other silicates are needed to quantify these effects.

Our data contain a wide-variety of spectral features between 40 and 80 μm which could be used to diagnose both the mineralogy, and the temperatures of specific grain populations if new observations with a far-infrared spectrometer on the proposed *Space Infrared Telescope for Cosmology and Astrophysics (SPICA)* were to be obtained. Such a study would provide a substantive link between the silicates min-

eralogists and meteoriticists analyse in the laboratory and the mineralogy inferred from astronomical observations.

ACKNOWLEDGEMENTS

JEB is supported by a 2-year *Science and Technology Research Council* Ernest Rutherford Returner Fellowship (ST/S004106/1). The measurements at WU by EK and AMH were supported by NSF-AST-9805924 and NASA APRA04-000-0041. We thank Dan Kremser of Washington University for the microprobe analyses.

DATA AVAILABILITY

The pyroxene spectra presented this article are subject to a partial embargo of 12 months from the publication date of the article during which the data will be available from the authors by request. Once the embargo expires the data will be available from <https://zenodo.org/communities/mineralspectra/>

REFERENCES

- Armstrong J., 1988, in Newbury D. E., ed., *Microbeam Analysis*. San Francisco Press, San Francisco, p. 469
- Bohren, C. F. & Huffman, D. R., *Absorption and scattering of light by small particles*. New York: Wiley, 1983
- Bregman, J. D., Hayward, T. L., Sloan, G. C. 2000 *ApJ*, 544, 75
- Hemingway, B. S., Bohlen, S. R., Hankins, W. B., Westrum, E. F., Kuskov, O. L., 1998, *Am Min*, 83, 409
- Bowey, J. E., Adamson A. J., 2002, *MNRAS*, 334, 94
- Bowey, J. E., Lee, C., Tucker, C., Hofmeister, A. M., Ade, P. A. R., Barlow, M. J., 2001, *MNRAS*, 325, 886
- Bowey, J. E. & Hofmeister, A. M. 2005, *MNRAS*, 358, 1383
- Bowey, J. E., Morlok, A., Köhler, M., Grady, M., 2007, *MNRAS*, 376, 1367
- Bowey J. E., Adamson A. J., Speck A. K., 2000, *ASP Conf. Ser.*, 196, 31
- Chen, R., Luo, A., Liu, J., Jiang, B., 2016, *AJ*, 151, 146.
- Chihara, H., Koike, C., Tsuchiyama, A., Tachibana, S., Sakamoto, D., 2002 *A&A*, 391, 267
- Deer, W. A., Howie, R. A., Zussman, J. *Rock-forming minerals*, Vol 2A: Single Chain Silicates, 2nd Ed, London : Longman 1978
- Do-Duy, T., Wright, C. M., Fujiyoshi, T., Glasse, A., Siebenmorgen, R., Smith, R., Stecklum, B., Sterzik, M., 2020, *MNRAS*, 493, 4463
- Ferraro J. R., 1982, *The Sadtler Infrared Spectra Handbook of Minerals and Clays*. Sadtler Research Laboratories
- Griffiths, P.R., and deHaseth, James A. *Fourier Transform Infrared Spectrometry*. John Wiley and Sons: New York 1986
- Goldman, D. S., Rossman, G. R., 1979, *Phys. Chem. Minerals* 4, 43
- Hanner, M. S., Lynch, D. K., Russell, R. W., 1994, *ApJ*425, 274
- Hofmeister, A. M., 2012, *European Journal of Mineralogy*, 24, 669
- Hofmeister, A. M. & Bowey, J. E., 2006, *MNRAS*, 367, 577
- Hofmeister, A. M., Keppel, E., Speck, A. K., 2003, *MNRAS*, 345, 16
- Hofmeister, A. M., Pitman, K., 2007, *Phys. Chem Minerals*, 34, 319
- Hofmeister, A. M., Pertermann, M., 2008 *Eur. J. Mineral*, 20, 537
- Hofmeister, A.M., Xu J., Mao H.-K., Bell P.M., Hoering, T.C. 1989 *Am Mineral* 74, 281

Huebner, J. S., Turnock, A. C. 1980, *Am Min* 65, 225
 Imai Y., Koike C., Chihara H., Murata K., Aoki T., Tsuchiyama A., 2009, *A&A*, 507, 277
 Jaeger, C., Molster, F. J., Dorschner, J., Henning, Th., Mutschke, H., Waters, L. B. F. M., 1998, *A&A*, 339, 904
 Johnson, N. M., 2002, PhD thesis, Washington University in St. Louis, Missouri, USA
 Johnson, N. M., Fegley, B., 2003 *Icarus*, 164, 317
 Koike, C., Noguchi, R., Chihara, H., Suto, H., Ohtaka, O., Imai, Y., Matsumoto, T., Tsuchiyama, A., 2013, *ApJ*, 778, 60
 Malfait, K., Waelkens, C., Waters, L. B. F. M., Vandebussche, B., Huygen, E., de Graauw, M. S. 1998, *A&A*, 332, L25
 Morimoto, N., Fabries, J., Ferguson, A. K., Ginzburg, I. V., Ross, M., Seifert, F. A., Zussman, J., Aoki, K., Gottardi, G., 1988, *Am Min* 73, 1123
 Okada A., Keil K., Taylor G. J., Newsom H., 1988, *Metic*, 23, 59
 Ormaasen, D. E., 1977, *Lithos*, 10, 291
 Pitman, K. M., Dijkstra, C., Hofmeister, A. M., Speck, A. K., 2010, *MNRAS*, 406, 460
 Speck, A. K., Wittington, A. G., Hofmeister, A. M., 2011 *ApJ*, 740, 93
 Sogawa, H., Koike, C., Chihara, H., Suto, H., Tachibana, S., Tsuchiyama, A., Kozasa, T. 2006, *A&A*, 451, 357
 Speck, A. K., Hofmeister, A. M., Barlow, M. J., 1999, *ApJ*, 513, 87
 Spoon, H. W. W., Tielens, A. G. G. M., Armus, L., Sloan, G. C., Sargent, B., Cami, J., Charmandaris, V., Houck, J. R., Soifer, B. T. 2006, *ApJ*, 638, 759
 Tamanai A., Mutschke H., Blum J., 2009, in Th. Henning, E. Grün, and J. Steinacker, eds. *ASP Conf Ser.*, Vol. 414, *Cosmic Dust- Near and Far*, Astron. Soc. Pac., San Francisco, p. 438
 Willett, K. W., Darling, J., Spoon, H. W. W., Charmandaris, V., Armus, L., 2011, *ApJS*, 193, 18
 Waters, L. B. F. M. et al. 1996, *A&A* 315, L361
 Wooden, D. H., Harker, D. E., Woodward, C. E., Butner, H. M., Koike, C., Witteborn, F. C., McMurtry, C. W., *ApJ*, 517, 1034
 Wooten F., 1972, *Optical properties of solids*. Academic Press, San Diego

APPENDIX A: ESTIMATED FILM THICKNESSES, MERGING POINTS AND QUARTZ CORRECTION

A1 Quartz correction in En_{12} and En_1

The spectrum of En_1 , the ferrosilite, Fe-end-member orthopyroxene has weak bands at $12.50 \mu\text{m}$, $12.82 \mu\text{m}$ (which are very weak in En_{12}) in addition to a very weak $14.37 \mu\text{m}$ band. These bands match the wavelengths of bands in α quartz (see Koike et al. 2013). Therefore we obtained a DAC spectrum of quartz, scaled it to the 12.5 and 12.8- μm features, and subtracted it from our mid-infrared data (Figure A1). These data were merged with the re-scaled far-infrared spectra before the band strength calibration. Quartz bands were not detected or subtracted from the far-infrared spectra.

This paper has been typeset from a $\text{T}_{\text{E}}\text{X}/\text{L}^{\text{A}}\text{T}_{\text{E}}\text{X}$ file prepared by the author.

Table A1. Mid-IR (450–4000 cm^{-1}) spectra were defringed and merged with scaled far-IR (80–650 cm^{-1}) spectra at point P1. In both cases the separation between data-points is about 0.5 cm^{-1} , unless otherwise specified. The 1–2 cm^{-1} -resolution specified in Section 3 describes how close peaks can lie but still be distinguished. In some spectra reflection artificially broadened the Si–O stretch near 1100 cm^{-1} : this was subtracted by fitting a curve to the unaffected spectrum of En_{55} and scaling this to the affected spectra at P2; the position of P2 was chosen so that real kinks in the data were not removed.

Sample	d (MIR) μm	P1 cm^{-1} (μm)	P2 cm^{-1} (μm)
En_{99}	0.25	582 (17.2)	1156 (8.6)
En_{92}	0.29	546 (18.3)	1150 (8.7)
En_{90}	0.38	595 (16.8)	–
En_{85}	0.86	519 (19.3)	– ^a
$\text{Wo}_{10}\text{En}_{62}$	0.87	484(20.7)	–
En_{55}	0.35	486 (20.6)	–
En_{40}	0.25	584 (17.1)	1116 (9.0)
En_{12}	0.44	471 (21.2)	1103 (9.1)
En_1	0.65	520 (19.2)	1102 (9.1)
<hr/>			
$\text{Wo}_{21}\text{En}_{79}$	0.78	482 (20.7)	1135 (8.8)
$\text{Wo}_{30}\text{En}_{70}$	0.53	469 (21.3)	1131 (8.8)
$\text{Wo}_{40}\text{En}_{60}$	0.48	527 (19.0) ^b	1131 (8.8)
<hr/>			
$\text{Wo}_{50}\text{En}_{50}$	0.71	458 (21.8)	1136 (8.8)
$\text{Wo}_{50}\text{En}_{47}$	0.19	490 (20.4) ^c	1144 (8.7)
$\text{Wo}_{49}\text{En}_{36}$	1.01	454 (22.0)	–
$\text{Wo}_{36}\text{En}_{37}$	0.46	442 (22.6)	–
$\text{Wo}_{47}\text{En}_6$	0.38	557 (18.0)	–
<hr/>			
$\text{Wo}_{99}\text{En}_1$	0.88	451 (22.2)	–

^a Defringing was not required; MIR resolution was 1 cm^{-1} ; FIR 0.5 cm^{-1}

^b data between 508 and 528 (18.9–19.7 μm) were interpolated due to difficulties with the merge; structure here is spurious.

^c MIR spectral resolution was 1.0 cm^{-1} , FIR: 0.5 cm^{-1}

Table A2. Mineral compositions for samples microprobed at Washington University

Sample Locality	$\text{Wo}_{49}\text{En}_{36}$ Calumet	$\text{Wo}_{47}\text{En}_6$ Iona Is.	$\text{Wo}_{36}\text{En}_{37}$ Belmont
<hr/>			
Oxide / per cent			
SiO_2	51.57	48	49.95
TiO_2	0.16	–	0.85
Al_2O_3	1.45	0.5	1.83
Cr_2O_3	–	–	0.01
Fe_2O_3	–	2	–
FeO	7.79	23	14.93
MnO	0.52	1	0.36
MgO	13.03	2	13.06
CaO	24.55	21	17.43
Na_2O	0.11	–	0.25
K_2O	–	–	–
H_2O^+	–	–	–
H_2O^-	–	–	–
Impurities			
<hr/>			
Total / per cent	99.18	97.5	98.67

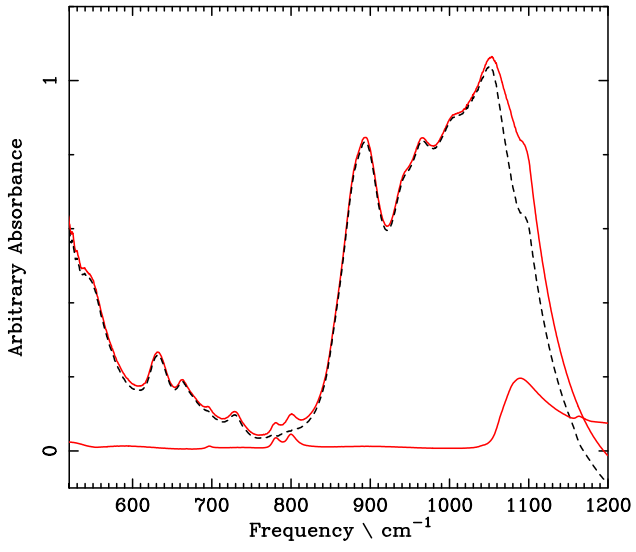


Figure A1. Removal of quartz impurity from En_1 spectrum. A quartz spectrum, scaled to bands at 12.5 and $12.82 \mu\text{m}$ (bottom solid red curve), was subtracted from the mid-infrared range of En_1 (black dashed line). The cleaned En_1 spectrum is the main solid red curve.